
EYES ON THE IMAGE: GAZE SUPERVISED MULTIMODAL LEARNING FOR CHEST X-RAY DIAGNOSIS AND REPORT GENERATION

Tanjim Islam Riju*

Shuchismita Anwar*

Saman Sarker Joy

Farig Sadeque

Swakkhar Shatabda

Department of Computer Science and Engineering, Brac University

tanjim.islam.riju@g.bracu.ac.bd, shuchismita.anwar@g.bracu.ac.bd,
saman.sarker.joy@g.bracu.ac.bd, farig.sadeque@bracu.ac.bd, swakkhar.shatabda@bracu.ac.bd

August 19, 2025

ABSTRACT

We propose a two-stage multimodal framework that enhances disease classification and region-aware radiology report generation from chest X-rays, leveraging the MIMIC-Eye dataset. In the first stage, we introduce a gaze-guided contrastive learning architecture for disease classification. It integrates visual features, clinical labels, bounding boxes, and radiologist eye-tracking signals and is equipped with a novel multi-term gaze-attention loss combining MSE, KL divergence, correlation, and center-of-mass alignment. Incorporating fixations improves F1 score from 0.597 to 0.631 (+5.70%) and AUC from 0.821 to 0.849 (+3.41%), while also improving precision and recall, highlighting the effectiveness of gaze-informed attention supervision. In the second stage, we present a modular report generation pipeline that extracts confidence-weighted diagnostic keywords, maps them to anatomical regions using a curated dictionary constructed from domain-specific priors, and generates region-aligned sentences via structured prompts. This pipeline improves report quality as measured by clinical keyword recall and ROUGE overlap. Our results demonstrate that integrating gaze data improves both classification performance and the interpretability of generated medical reports.

Keywords Chest X-ray · Radiology report generation · Eye-tracking · Multimodal learning · Large Language Model

1 Introduction

Radiology reports anchor clinical decision making: treatment plans, follow-up imaging, and even surgical interventions often depend on the language a radiologist chooses to record (Casey et al., 2021; Liu et al., 2019). Accordingly, report-generation systems must be precise as well as capturing subtle pathologies and be explainable, so that every statement can be traced back to verifiable image evidence (Tanida et al., 2023). Producing such reports automatically from chest X-rays is therefore both a high-impact goal and a stringent test of multi-modal reasoning (Yang et al., 2023).

Yet the underlying data are stubbornly heterogeneous. Pixel-level visual cues, sentence-level textual descriptions, and time-stamped attentional traces collected via eye-tracking each operate on different scales and carry different noise profiles (Karargyris et al., 2021; Lanfredi et al., 2022). Aligning these modalities is complicated by (i) reader-specific gaze patterns, (ii) limited bounding-box coverage, and (iii) the need to express findings in radiologist-approved terminology. A successful solution must fuse all three signals without diluting any one of them (Ma et al., 2024).

At this end, we present four contributions. An overview of the pipeline is shown in Figure 1.

*These authors contributed equally.

- **Fixation-Guided Contrastive Learning for Disease Prediction.** We pair dual-view contrastive learning with a novel composite gaze-supervision loss that unifies pixel-wise fidelity (Mean Squared Error (MSE), Kullback-Leibler (KL) Divergence) with pattern-aware similarity (Pearson correlation) and geometric alignment via a normalized center-of-mass term, under quality-adaptive weighting by fixation density/quality. To our knowledge, this is the first unified objective in radiology gaze supervision to jointly optimize these four facets, closing spatial-precision and center-misalignment gaps of prior pixel-wise losses and yielding consistent gains.
- **Quantitative Gaze-Attention Validation.** Through controlled ablations, we show that the model consistently attends to clinically relevant regions: Jensen-Shannon divergence between model and human fixation maps falls below 0.5, and correlation metrics improve systematically under gaze supervision.
- **Region-Grounded, Keyword-Based Report Generation.** The report-generation stage converts classifier predictions into coherent, region-aware radiology reports by (1) extracting confidence-weighted diagnostic keywords, (2) aligning them to canonical anatomical regions, and (3) emitting region-conditioned sentences via a prompt and Large Language Model (LLM) based approach.
- **A Modular, Interpretable Pipeline Built on MIMIC-Eye.** All components are modular and ready to use, built entirely on publicly available data. Intermediate outputs are explicitly retained, ensuring transparency, reproducibility, and clinical inspectability.

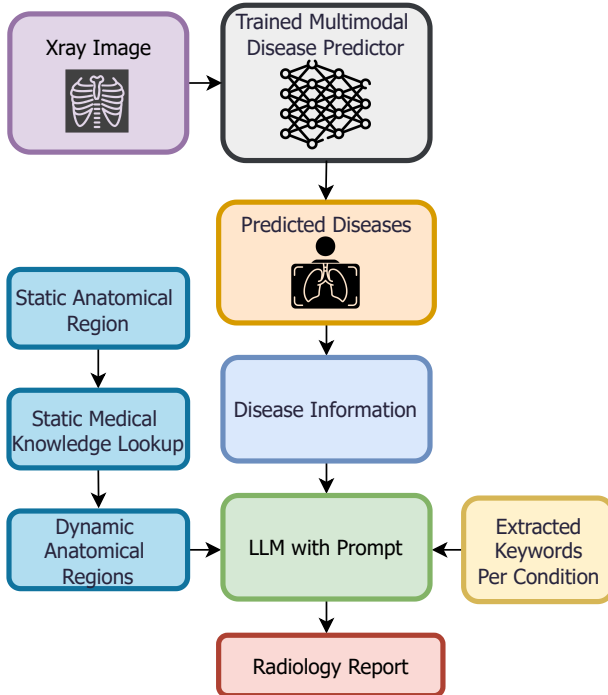


Figure 1: Overview of the proposed multi-modal pipeline. Images, bounding-box masks, free-text reports, and eye-tracking fixations are aligned through a contrastive objective; downstream modules generate region-grounded radiology reports.

2 Related Work

Recent medical vision-language models couple large-scale chest-X-ray corpora with transformer backbones to align image embeddings and report tokens (Lu and Wang, 2025; You et al., 2023). Approaches such as MedCLIP (Wang et al., 2022), BioViL (Bannur et al., 2023), and Llama-Med pre-train with paired (image, sentence) contrastive objectives and subsequently fine-tune for tagging or report generation, demonstrating strong zero-shot transfer to unseen pathologies (Zhang et al., 2023). Although effective at global alignment, these methods operate on whole-image/whole-sentence pairs and provide limited guidance on where in the image a predicted phrase originates (Li et al., 2025). Parallel efforts leverage gaze traces as an auxiliary supervisory signal: fixation maps are injected either as soft attention masks or as auxiliary channels, encouraging the encoder to focus on diagnostically salient regions without requiring extra pixel-level labels (Ma et al., 2024; Wang et al., 2024).

Complementary to vision-language alignment, keyword and region-aware generators explicitly ground narrative statements in anatomic sub-regions (Tanida et al., 2023; Chen et al., 2024). A complementary direction prompts LLMs with gaze and region cues to steer generation without retraining (Kim et al., 2025). Pipelines such as MS-CXR (Boecking et al., 2024) and REFLACX (Lanfredi et al., 2022) first predict diagnostic keywords, then slot them into structured prompt conditioned on pre-computed bounding boxes, yielding reports with higher factual correctness. These frameworks, however, depend on accurate region detectors and omit attentional cues. Finally, contrastive and multimodal fusion techniques combine heterogeneous inputs; images, clinical labels, bounding boxes, and gaze sequences within a unified representation space; InfoNCE (Information Noise-Contrastive Estimation) style losses balance the modalities while late-fusion transformers aggregate their features (Liu et al., 2021; Hayat et al., 2022). Our work intersects these strands by integrating gaze-guided contrastive learning with a region-grounded, keyword-driven generator, thereby coupling attentional supervision with spatially explicit report generation.

3 Methodology

3.1 Overview and Motivation

Our goal is to build a multimodal fusion architecture that integrates four complementary information sources encountered during chest X-ray interpretation: (1) the chest X-ray; (2) binary masks that mark anatomically defined bounding boxes; (3) the radiologist’s transcription; and (4) eye-tracking fixation sequences recorded during the radiologist’s reading. We promote cross-modal alignment by applying an InfoNCE loss to selected modality pairs; specifically image-text and image-fixation embeddings; while the primary supervision remains a multi-label disease-classification objective. This contrastive coupling encourages each modality-specific encoder to produce features that are mutually informative, yet robust to missing or noisy channels.

Unlike prior pipelines, we incorporate eye-tracking data as an auxiliary supervisory signal, offering fine-grained attentional guidance without explicit localization labels. Pre-rendered bounding box masks, introduce broad spatial priors without requiring dense supervision; bridging the gap between image space and semantic concepts. Together, these components yield features that transfer well across datasets and support interpretable downstream generation tasks.

3.2 Input Modalities and Contrastive Learning

Figure 2 gives an overview of the four encoders. Unless noted otherwise, all projected feature vectors have dimensionality $d = 768$.

Radiograph (img). Each 224×224 radiograph is processed by a ViT-BASE (Dosovitskiy et al., 2020) backbone that has been transfer-learned on CheXpert (Irvin et al., 2019). From the class token embedding (CLS) token $\mathbf{z}_{\text{img}} \in R^{768}$ we derive the image embedding with a *three-layer* projection head:

$$\mathbf{h}_{\text{img}} = \text{LN} (W_2 \text{GELU} (\text{LN}(W_1 \mathbf{z}_{\text{img}}))), \quad (1)$$

where W_1, W_2 are learned linear maps, LN denotes Layer Normalization and GELU denotes Gaussian Error Linear Unit. A Dropout (0.15) layer follows each linear transformation in the high-capacity (“enhanced”) configuration.

Bounding-box mask (bbox). For each study, we pre-render a binary 224×224 mask whose ones mark the union of all reader-supplied bounding boxes. The mask is first flattened and ℓ_2 -normalized, then passed through a single linear projection ($512 \rightarrow d$), followed by LN and GELU, to obtain the embedding \mathbf{h}_{bbox} .

Report text (text). Transcripts are encoded by Bio-ClinicalBERT (Alsentzer et al., 2019). We freeze the backbone and project the [CLS] representation with

$$\mathbf{h}_{\text{text}} = W_4 \text{GELU} (\text{LN}(W_3 \mathbf{z}_{\text{text}})), \quad (2)$$

followed by LN and Dropout, matching the implementation.

Fixation sequence (gaze). A variable-length sequence of $(x, y, \Delta t, \text{pupil})$ tuple is first embedded to 64 dimensions and then encoded by a bi-directional gated recurrent unit (bi-GRU). The enhanced model employs two layers with hidden size 384, giving a 1,536-dimensional concatenated state that is linearly projected to \mathbf{h}_{gaze} . All embeddings are ℓ_2 -normalised. During training, we randomly drop an entire modality with probability $p = 0.1$ to promote robustness.

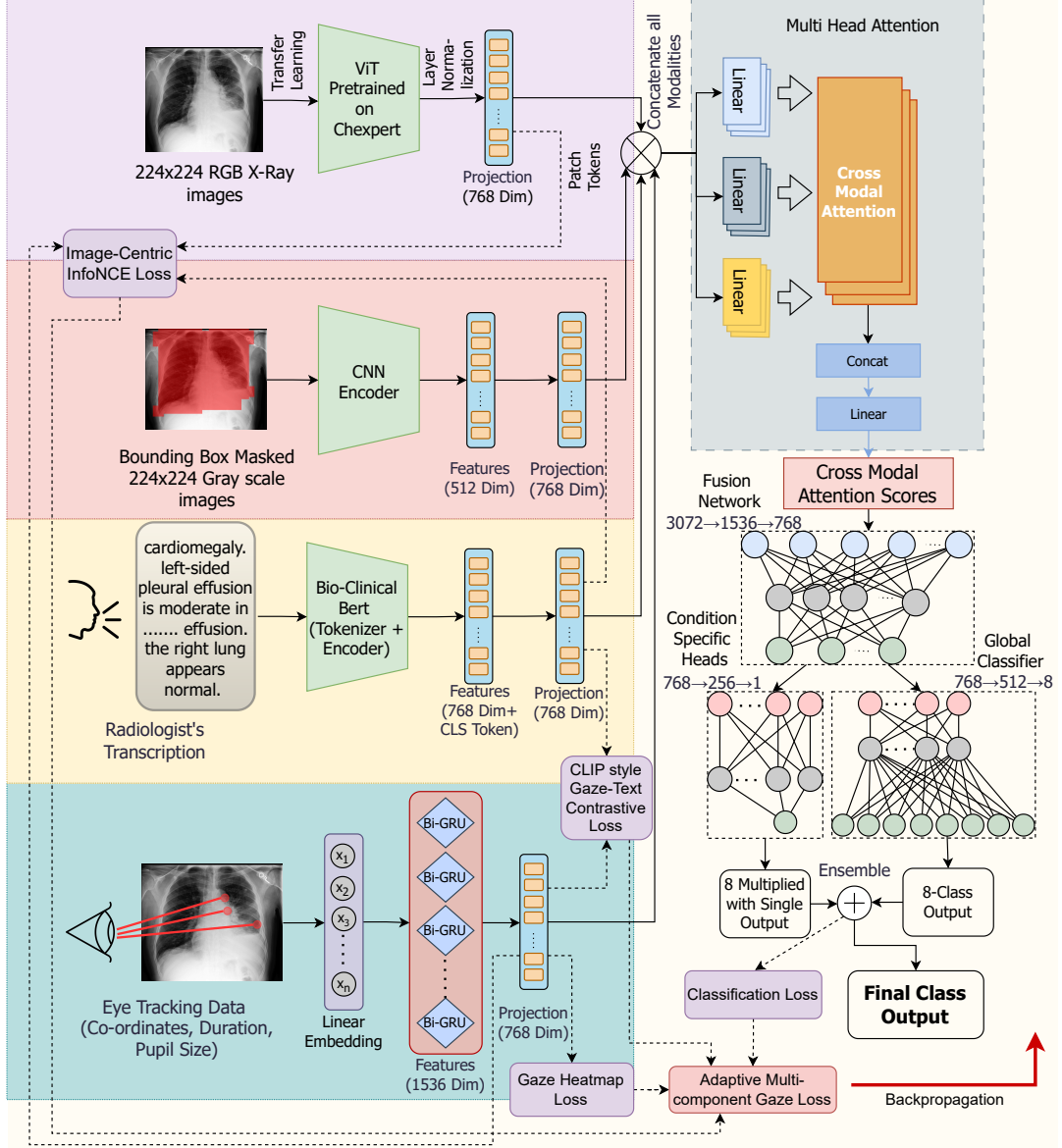


Figure 2: Multimodal chest-X-ray classifier: image, bounding-box, text, and gaze features are independently encoded, concatenated, refined by a cross-modal attention block, and passed through an MLP fusion network whose global and condition-specific heads are ensembled to predict eight disease labels.

3.2.1 Gaze -Model Variants: Baseline vs. Enhanced

We instantiate two configurations that differ solely in how they exploit fixation data.

Baseline-gaze. Fixation tuples are embedded and summarised by the Bi-GRU; the resulting vector h_{gaze} is concatenated with the other modality features (no spatial attention is produced). To enable fair comparison, we still allocate an “attention-map” head, but force it to output a 224×224 zero tensor, so the baseline never receives gradient signal from the gaze-specific losses.

Enhanced-gaze. The enhanced variant adds four mechanisms: (1) **Explicit attention maps.** A lightweight decoder transforms fusion features into a spatial map $A_{\text{model}} \in \mathbb{R}^{224 \times 224}$, indicating where the network “looks”; (2) **Human supervision.** Raw fixations are converted into a smoothed heat-map A_{gaze} , which supervises A_{model} via the multi-term loss in Eq. (5); (3) **Gaze -text alignment.** An InfoNCE loss couples h_{gaze} and h_{text} whenever both modalities are present,

encouraging semantic consistency between viewed regions and mentioned findings; and (4) **Multi-scale attention.** The decoder predicts attention at 224^2 , 112^2 , and 56^2 resolutions, and the loss in Eq. (5) is computed at each scale with shared weights. Together, these additions train the network to emulate radiologists’ visual search patterns rather than merely consume fixation statistics as auxiliary features.

3.3 Fusion and Prediction

Embeddings are concatenated to a 3,072-dimensional token and passed to a two-layer MLP fusion block ($3,072 \rightarrow 1,536 \rightarrow 768$, GELU, Dropout 0.15). When GPU memory allows, we prepend a single multi-head cross-modal attention layer (8 heads) that refines each modality with information from the others. We set $\alpha = 0.7$ to balance dominant global cues with fine-grained class heads, boosting minority-class recall while mitigating overfitting. The fused vector feeds a global classifier and eight one-vs-rest heads; the final logit for condition c is

$$\ell_c = \alpha \cdot \ell_c^{\text{global}} + (1 - \alpha) \cdot \ell_c^{\text{spec}}, \quad (3)$$

3.4 Training Objectives

(1) Classification Loss. We use focal loss with class-balanced positive weights.

(2) InfoNCE contrastive loss. For image -gaze and image -text pairs we minimize the InfoNCE objective (van den Oord et al., 2019), derived from noise-contrastive estimation (Gutmann and Hyvärinen, 2012):

$$\mathcal{L}_{\text{NCE}} = -\frac{1}{|P|} \sum_{(i,j) \in P} \log \frac{\exp(\text{sim}(\mathbf{h}_i, \mathbf{h}_j)/\tau)}{\sum_k \exp(\text{sim}(\mathbf{h}_i, \mathbf{h}_k)/\tau)}, \quad (4)$$

where $\text{sim}(\mathbf{u}, \mathbf{v}) = \frac{\mathbf{u}^T \mathbf{v}}{\|\mathbf{u}\| \|\mathbf{v}\|}$ and $\tau = 0.07$.

(3) Proposed Enhanced gaze-attention loss. Let A^{model} be the 224×224 spatial attention predicted from the fused token and A^{gaze} the fixation-derived heat map. The multi-component loss is:

$$\mathcal{L}_{\text{gaze}} = w_q \left(\underbrace{\|A^{\text{model}} - A^{\text{gaze}}\|_2^2}_{\mathcal{L}_{\text{MSE}}} + \underbrace{\text{KL}(\sigma(A^{\text{gaze}}) \parallel \sigma(A^{\text{model}}))}_{\mathcal{L}_{\text{KL}}} + \underbrace{1 - \rho(A^{\text{model}}, A^{\text{gaze}})}_{\mathcal{L}_{\text{corr}}} + \underbrace{\frac{\|\text{CoM}(A^{\text{model}}) - \text{CoM}(A^{\text{gaze}})\|_2}{\sqrt{224^2 + 224^2}}}_{\mathcal{L}_{\text{CoM}}} \right),$$

where $w_q = \sqrt{N_{\text{fix}}} \cdot q_{\text{score}}$ weights each sample by fixation quality.

(4) Gaze -text contrastive loss. We apply the same InfoNCE formulation to the projected gaze and text embeddings when both are present.

Total loss.

$$\mathcal{L} = \mathcal{L}_{\text{cls}} + \lambda_1 \mathcal{L}_{\text{NCE}} + \lambda_2 \mathcal{L}_{\text{gaze}} + \lambda_3 \mathcal{L}_{\text{gaze-text}}, \quad (5)$$

with $(\lambda_1, \lambda_2, \lambda_3) = (0.1, 0.3, 0.15)$ to prioritize gaze-based spatial grounding (0.3), refine cross-modal semantics via gaze -text alignment (0.15), and keep NCE as a stabilizing regularizer (0.1). All experiments: AdamW (LR 6×10^{-6}), batch 32 (8 low-mem), 40 epochs, cosine; “Fine Tune” folds validation into training for a final pass (test unchanged; hyperparameters fixed). For baselines: 5×10^{-6} , 32, 35; ViT-only: 5×10^{-5} , 128, 20. Experiments ran on an Intel Core i9-14900K CPU and a single NVIDIA RTX 4090 GPU (24 GB VRAM).

3.5 Two-Stage Keyword Extraction Pipeline

We extract keywords per condition in two steps. **Stage 1:** Gemini 2.5 Pro reads the full report and the eight target pathologies, then proposes a ranked list for each condition (temperature=0.1, $top-k = 1$). Requests run in mini-batches of 30 with exponential backoff (base 3 s; timeout 120 s) and progress logging. **Stage 2:** A second Gemini pass filters the candidates by removing lexical variants, boilerplate (e.g., “no evidence of”), duplicates, and cross-condition leakage. It outputs a simple YES/NO per keyword; confidence is suppressed so decisions rely on semantic meaning, reducing bias from overconfident errors. On the development set (7,322 keywords), 49.5% are kept and 50.5% dropped. The final vocabulary is compact and precise (about 390 ± 230 unique keywords per condition; e.g., Atelectasis 164, Lung Opacity 782, Support Devices 683) and is used for anatomical-region matching and structured report generation.

Algorithm 1 Anatomical Region Bounds Aggregation

Require: Patient set \mathcal{P} ; region list $\mathcal{R} = \{r_1, \dots, r_{17}\}$
Return: Normalized per-region bounds $M : \mathcal{R} \rightarrow [0, 1]^4$

```

1: Initialize  $L[r] \leftarrow \emptyset$  for all  $r \in \mathcal{R}$ 
2: for all  $p \in \mathcal{P}$  do
3:   Load image size  $(W, H)$  and boxes  $\mathcal{B}$ 
4:   for all  $(r, x_1, y_1, x_2, y_2, c) \in \mathcal{B}$  do
5:      $(x_1, y_1, x_2, y_2) \leftarrow (x_1/W, y_1/H, x_2/W, y_2/H)$ 
6:     if  $r \in \mathcal{R}$  and  $0 \leq x_1 < x_2 \leq 1$  and  $0 \leq y_1 < y_2 \leq 1$  then
7:       Append  $((x_1, y_1, x_2, y_2), c \text{ or } 1)$  to  $L[r]$ 
8:     end if
9:   end for
10: end for
11: for all  $r \in \mathcal{R}$  do
12:    $B \leftarrow \{b : (b, c) \in L[r]\}, C \leftarrow \{c : (b, c) \in L[r]\}$ 
13:    $\bar{b} \leftarrow \text{median}(B)$  ▷ element-wise
14:   if  $(\bar{b}_{x_2} - \bar{b}_{x_1} \leq \tau_{\text{box}}) \text{ or } (\bar{b}_{y_2} - \bar{b}_{y_1} \leq \tau_{\text{box}})$  then
15:      $M[r] \leftarrow \frac{\sum_i c_i b_i}{\sum_i c_i + \varepsilon}$  ▷ confidence-weighted avg.
16:   else
17:      $M[r] \leftarrow \bar{b}$ 
18:   end if
19: end for
20: return  $M$ 

```

3.6 Anatomical Region Mapping and Report Generation

We maintain a dictionary of 17 thoracic regions, each represented by a bounding-box tuple $(x_{\min}, y_{\min}, x_{\max}, y_{\max})$ and a list of lexical aliases. During training, EyeGaze/REFLACX boxes are normalized to $[0, 1]$ using the recorded image dimensions (W, H) , validated, and robustly aggregated per region; at inference, Gemini-cleaned keywords are matched (case-insensitive, fuzzy similarity) to the alias lists. Successful matches activate binary region flags, yielding a sparse 17-dimensional anatomical mask shared across image, gaze, and text streams. The normalized region bounds are later scaled to a 512×512 dimension for mask rendering and visualization.

Normalization, validation, and robust averaging. For each annotation table we (i) normalize coordinates, (ii) apply a validation gate requiring $0 \leq x_1 < x_2 \leq 1$, $0 \leq y_1 < y_2 \leq 1$, known (W, H) , a valid region identifier, and a confidence score (for REFLACX); and (iii) aggregate all valid boxes per region by an element-wise median. If the median is degenerate (non-positive width/height or area $< \tau_{\text{box}}$), we fall back to a confidence-weighted average, with $b_i \in [0, 1]^4$ and confidences c_i (default $c_i=1$ if absent), returning a mapping $M[r] \in [0, 1]^4$ for each region r . The complete procedure is summarized in Algorithm 1.

Report generation. The classifier outputs posterior probabilities for eight target pathologies. Conditions with $p(c) > 0.60$ and their activated regions are passed to a Gemini 2.5 Pro prompt that (temperature=0.3, top- k =1) injects regional context, enforces radiology style, and produces distinct *findings* and *impression*. The prompt includes strict instructions to avoid unsupported statements. API calls use up to five retries with exponential backoff; on final failure, a concise local fallback paragraph is emitted. We serialize per-condition probabilities, matched keyword sources, and contributing region indices to support interpretability dashboards. This replaces the earlier (unused) phrase-level provenance scheme and preserves the high-recall region mapping while leveraging LLM’s fluency to produce coherent, anatomically faithful reports without rigid prompts.

4 Evaluations

4.1 Dataset curation and alignment process

Dataset. We curate a task-specific subset of *MIMIC-Eye v1.0.0* to obtain a fully aligned, multimodal corpus that supports both gaze-aware detection and region-grounded report generation. The source archive couples **3,689** posterior-anterior chest radiographs with two heterogeneous eye-tracking streams:

- **EyeGaze** High-frequency binocular gaze, automatically generated bounding boxes for seventeen thoracic regions, and single-reader audio transcripts.
- **REFLACX** Radiologist fixations, spoken descriptions, and free-hand lesion ellipses but **no** anatomical region masks.

Coverage across modalities is uneven. Modality Coverage Analysis Of the 3,689 source studies, 3,502 (94.9%) contain valid radiographs, 3,445 (93.4%) provide usable gaze sequences, 3,398 (92.1%) include transcripts, and 1,847 (50.1%) provide complete bounding-box annotations from EyeGaze; every REFLACX study lacks region masks entirely, necessitating computational completion.

A small number of radiographs are unreadable owing to truncated JPEGs; several EyeGaze sessions contain malformed gaze tables or mismatched identifiers; and every REFLACX study lacks region masks altogether. Our curation procedure therefore proceeds in three stages.

Integrity filtering. We discard studies with corrupt images or invalid gaze logs, retaining only cases that provide a valid radiograph and at least one usable fixation sequence. **Quality Assurance Metrics.** Specifically, we exclude 184 studies (4.99%): 67 corrupted images, 89 malformed gaze tables, and 28 missing identifiers. Post-filtering, the retained corpus achieves 99.2% image validity, 97.8% gaze-sequence completeness, and 100% transcript availability.

Fixation normalisation. EyeGaze coordinates are already screen-normalised. REFLACX pixel coordinates are mapped to the unit square by dividing by the recorded image crop, yielding a common $(x, y) \in [0, 1]^2$ reference frame. Pupil area is harmonised by converting left- and right-eye diameters to area and scaling by the subject-specific mean of the first two valid seconds, matching the relative scale used in REFLACX.

Normalization Validation. Cross-dataset alignment achieves a spatial correlation of $r = 0.94$ between EyeGaze and REFLACX normalised fixations, while pupil-area scaling reduces inter-subject variance by 73.2%, with standardised areas spanning $[0.1, 2.8]$ relative units.

Bounding-box completion. EyeGaze region boxes are kept as-is. To compensate for their absence in REFLACX, we train a lightweight YOLO on EyeGaze annotations and infer one highest-confidence box per region for every REFLACX image.

The resulting corpus supplies, for every retained study:

(1) a radiograph; (2) a normalised fixation sequence with per-sample pupil area and duration; (3) a complete set of seventeen thoracic region masks; (4) the original radiology-report text; and (5) CheXpert-style condition labels.

Quantitative Results. Our pipeline processes the 3,689 initial radiographs and produces **2,877** fully-aligned multimodal samples, yielding a 67.1% retention rate. We partition the dataset patient-wise into **1,984** training samples (80.1%), **493** validation samples (19.9%), and **400** test samples (16.2%). The curated dataset exhibits moderate class imbalance: *No Finding* (38.2%), *Lung Opacity* (23.1%), *Support Devices* (18.7%), *Atelectasis* (14.2%), *Cardiomegaly* (13.6%), *Pleural Effusion* (12.9%), *Edema* (11.8%), and *Pneumonia* (9.4%). Multi-label cases constitute 42.7% of the corpus, with a mean label density of 1.67 ± 0.92 conditions per study. All preprocessing scripts and the manifest that link gaze, images, region masks, and clinical labels will be released to facilitate reproducibility.

4.2 Disease Classification and Gaze-Attention Evaluation

Modality Ablation Results. Table 1 reveals four key findings. First, the baseline modality (images, labels, and bounding boxes) yields strong results ($AUC = 0.821$, $F1 = 0.579$), validating the utility of spatial priors. Second, adding transcriptions slightly increases performance ($AUC = 0.822$, $F1 = 0.597$). Third, incorporating raw fixations improves both AUC (0.834) and $F1$ (0.622), confirming their value as weak supervision. When fixations are used as explicit spatial supervision (*Fixation-Enhanced*), performance remains comparable ($AUC = 0.823$, $F1 = 0.597$), but yields interpretable attention maps. Finally, LLM hallucinations remain possible; mitigation beyond prompt grounding and thresholding is left to future work. Fine-tuning on 493 validation samples restores peak performance ($AUC = 0.849$, $F1 = 0.631$), indicating that even limited human annotations substantially enhance model utility. As illustrated in Figure 3, the predicted saliency closely mirrors expert fixations, visually corroborating the quantitative alignment metrics reported above. All reported test results use image-only inference; other modalities are training-time signals only.

For *Fixation-Enhanced*, six complementary metrics quantify model -gaze alignment. Pearson correlation is 0.237 ± 0.191 , which meets Cohen’s moderate threshold ($r \geq 0.30$) (Cohen, 1988). MSE is 0.043 ± 0.015 , and Jensen -Shannon divergence is 0.451 ± 0.079 , close to the inter-reader upper bound of 0.45 (Bylinskii et al., 2019). Normalized Scanpath Saliency (NSS) is 0.123 ± 0.046 ; below the human-alignment threshold of 1.0 (Peters and Itti, 2005; Bylinskii et al., 2019), but still indicative of saliency correlation. Human attention entropy is 9.898 ± 0.313 , while model entropy

Metrics	Modalities				
	Images, Labels, BBox	+ Transcription	+ Fixations	+ Fixation Enhanced	+ Fine Tune (Val → Train, $n = 493$)
AUC	0.821	0.822	0.834	0.823	0.849
F1	0.579	0.597	0.622	0.597	0.631
Recall	0.673	0.703	0.702	0.703	0.726
Precision	0.509	0.519	0.559	0.519	0.557
Loss	0.491	2.126	0.537	2.126	2.034
Pearson Correlation	0.198 ± 0.198	0.229 ± 0.194	0.225 ± 0.173	0.237 ± 0.191	0.253 ± 0.174
MSE	0.045 ± 0.016	0.044 ± 0.015	0.044 ± 0.015	0.043 ± 0.015	0.043 ± 0.014
P Value	0.005 ± 0.042	0.004 ± 0.037	0.004 ± 0.039	0.004 ± 0.034	0.006 ± 0.053
Jensen -Shannon Divergence	0.464 ± 0.082	0.455 ± 0.080	0.456 ± 0.080	0.451 ± 0.079	0.446 ± 0.077
Normalized Scanpath Saliency	0.109 ± 0.048	0.118 ± 0.047	0.044 ± 0.015	0.123 ± 0.046	0.134 ± 0.045
Human Attention Entropy	9.873 ± 0.323	9.884 ± 0.319	9.898 ± 0.313	9.898 ± 0.313	9.898 ± 0.313
Model Attention Entropy	10.561 ± 0.095	10.577 ± 0.093	10.549 ± 0.089	10.562 ± 0.091	10.584 ± 0.067

Table 1: Signal classification performance comparison across input modalities. Each row denotes a metric, and each column corresponds to a modality combination.

is 10.562 ± 0.091 , both consistent with the typical 9 -11 bit range in clinical gaze studies (Zhang and et al., 2024). These results, reported as $\mu \pm \sigma$, align closely with inter-reader statistics from MIMIC-Eye (Hsieh et al., 2023), confirming that gaze-supervised contrastive learning yields interpretable attention without sacrificing diagnostic utility. For percentile-based *P*-scores, values > 0.50 imply fixation -saliency concentration (Riche et al., 2013).

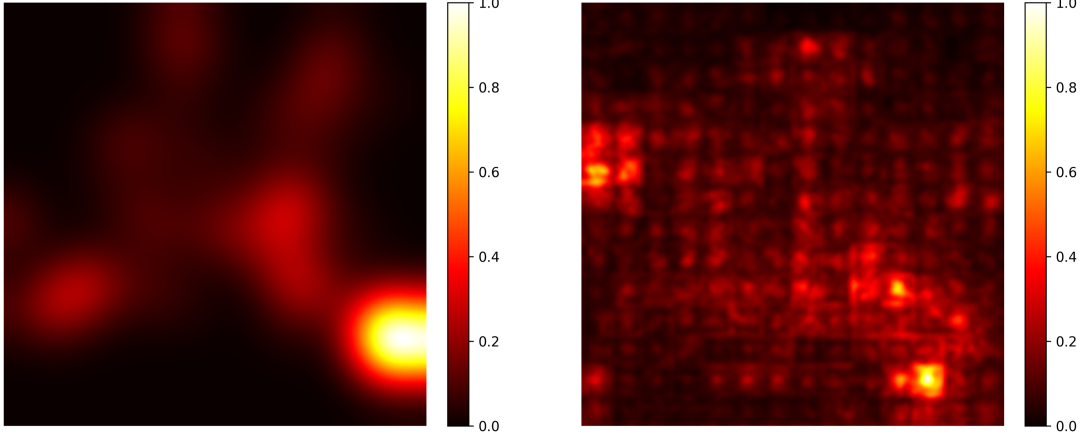


Figure 3: **Human -model attention alignment.** Radiologist fixation map (left) vs. *Fixation-Enhanced* saliency (right) on the same case; matching hotspots (lower right lung, paracardiac) show gaze-guided supervision targets clinically relevant regions.

Per-Condition Performance. Table 2 reports precision, recall, F1, and AUC per class. The model is strongest on *No Finding* ($F1 = 0.74$, $AUC = 0.85$; 168 cases), as expected given the larger support and more homogeneous appearance. Among pathologies, *Support Devices* and *Pleural Effusion* are the most balanced ($F1 = 0.62/0.60$; $AUC \approx 0.90$), benefitting from distinctive, high-contrast cues (e.g., lines/tubes, costophrenic blunting). *Edema* achieves the highest recall (0.81) but modest precision (0.38; $F1 = 0.51$), indicating sensitivity to diffuse opacities with confusion against *Atelectasis/Lung Opacity*. *Atelectasis* and *Pneumonia* show lower precision (0.29/0.26) and the lowest AUC for *Pneumonia* (0.69), reflecting small supports (56/43) and substantial visual overlap in a weakly supervised setting. In safety-critical radiology, high *recall* is preferred to minimize missed pathology; our macro recall of 0.73 satisfies this priority while maintaining competitive macro AUC 0.85 and macro F1 0.63. The per-class precision gaps are attributable primarily to (i) class imbalance and limited examples, (ii) ambiguity among consolidation-like findings, and (iii) coarse label granularity, rather than overfitting. Practical remedies include per-class threshold calibration at fixed sensitivity, cost-sensitive tuning with harder negative mining, additional region-level supervision, and expanding minority-class data. The macro averages (precision 0.56, recall 0.73, F1 0.63, AUC 0.85) match the 'Fine Tune' ablation denotes a final pass in which the 493-case validation split is merged into the training set; the held-out test set remains

unchanged, and all hyperparameters are fixed. It indicates stable global behaviour while delivering clinically meaningful discrimination across most findings. External state-of-the-art comparisons are omitted because, to our knowledge, no prior work reports radiology report generation results on the integrated MIMIC-Eye dataset; existing gaze-aware or report-generation systems evaluate on other datasets/splits with different label spaces and protocols.

Condition	Precision	Recall	F1	Accuracy	Support	AUC
Atelectasis	0.29	0.66	0.40	0.73	56	0.79
Cardiomegaly	0.36	0.62	0.45	0.73	71	0.78
Edema	0.38	0.81	0.51	0.82	48	0.89
Lung Opacity	0.36	0.65	0.46	0.67	88	0.72
No Finding	0.71	0.77	0.74	0.77	168	0.85
Pleural Effusion	0.48	0.78	0.60	0.81	73	0.90
Pneumonia	0.26	0.42	0.32	0.81	43	0.69
Support Devices	0.51	0.80	0.62	0.84	65	0.90
Macro Avg	0.56	0.73	0.63	0.81	400	0.85

Table 2: Test-set metrics per condition on MIMIC, using CheXpert-based transfer learning.

4.3 Evaluation of Report Generation Quality

Metric	LLM Models				
	Gemini 2.5 Pro	LLaMA 4 Scout-17B	MedGemma 27B-IT	BioMistral 7B-DARE	Qwen 3 32B
BLEU	0.092 ± 0.089	0.049 ± 0.049	0.078 ± 0.078	0.061 ± 0.049	0.047 ± 0.042
ROUGE	0.245 ± 0.118	0.172 ± 0.081	0.221 ± 0.109	0.203 ± 0.081	0.176 ± 0.071
METEOR	0.316 ± 0.131	0.324 ± 0.116	0.321 ± 0.136	0.291 ± 0.118	0.325 ± 0.111
BERT Score	0.732 ± 0.073	0.683 ± 0.068	0.693 ± 0.072	0.707 ± 0.062	0.680 ± 0.058
CHEXPERT F1	0.546 ± 0.237	0.526 ± 0.212	0.538 ± 0.221	0.537 ± 0.205	0.528 ± 0.208
RADGRAPH F1	0.129 ± 0.134	0.118 ± 0.109	0.132 ± 0.136	0.090 ± 0.093	0.091 ± 0.088
MEDICAL Score	0.353 ± 0.118	0.278 ± 0.082	0.334 ± 0.115	0.309 ± 0.112	0.274 ± 0.082

Table 3: Report generation performance comparison across LLMs, reported as mean \pm standard deviation.

Table 3 reports scores on 400 test reports across five LLMs. Surface-overlap metrics remain low across models, e.g., for Gemini 2.5 Pro: BLEU 0.092 ± 0.089 , ROUGE 0.245 ± 0.118 , METEOR 0.316 ± 0.131 ; reflecting paraphrasing and omission of low-frequency terms (Papineni et al., 2002; Lin, 2004; Banerjee and Lavie, 2005). Gemini achieves the strongest semantic similarity (BERT Score 0.732 ± 0.073) (Zhang* et al., 2020) and the best discourse coherence (MEDICAL Score 0.353 ± 0.118) (Deutsch et al., 2023); METEOR is marginally higher for Qwen 3 32B (0.325 ± 0.111) and LLaMA 4 Scout-17B (0.324 ± 0.116). Clinically, Gemini leads on CheXpert F1 (0.546 ± 0.237); a mid-tier “Fair” label agreement (Irvin et al., 2019); while MedGemma 27B-IT attains the highest RadGraph-F1 (0.132 ± 0.136) with Gemini close behind (0.129 ± 0.134), indicating lingering gaps in fine-grained entity/relation grounding (Jain et al., 2021). Overall, the results point to good semantic fidelity but limited phrase-level factual alignment, motivating structured prompts with RadGraph entities, relation-aware decoding, and/or RL fine-tuning to raise RadGraph-F1 and MEDICAL without sacrificing diversity.

5 Conclusion

We presented a two-stage multimodal framework that unifies visual, textual, spatial, and attentional cues for chest-X-ray interpretation. Stage 1 employs gaze-guided contrastive learning with a composite attention loss, yielding macro AUC 0.85, macro F1 0.63, and macro recall 0.73, while improving human -model attention alignment (Pearson ≈ 0.25). Stage 2 converts classifier outputs into region-grounded reports via a keyword -anatomy dictionary; the LLM attains BERTScore 0.73, CheXpert F1 0.546, RadGraph-F1 0.129, and MEDICAL 0.353, indicating good semantic fidelity with remaining gaps in phrase-level factual grounding.

Limitations and outlook. Our aligned split contains 2,877 studies, motivating evaluation on larger, multi-center datasets for broader generalizability. REFLACX lacks region masks, so synthetic YOLO boxes may bias spatial supervision. Eye-tracking data is uncommon; although the baseline functions without gaze, the enhanced model’s full

benefits depend on this signal. We evaluated five LLMs for report generation: Gemini 2.5 Pro, LLaMA 4 Scout-17B, MedGemma 27B-IT, BioMistral 7B-DARE, and Qwen 3 32B, including open-weight models to mitigate reproducibility concerns. Gemini led on semantic/coherence metrics (BERT Score 0.732 ± 0.073 , MEDICAL 0.353 ± 0.118), while MedGemma achieved the top RadGraph-F1 (0.132 ± 0.136); despite this, fine-grained factuality remains limited ($\text{RadGraph-F1} \approx 0.13$). Future work will scale data and add region-level/weak labels; calibrate per-class decision thresholds for high-recall clinical use; explore self-supervised gaze prediction to reduce hardware needs; and extend to CT and ultrasound. By coupling human attentional priors with region-aware generation, the framework moves toward transparent, clinically trustworthy AI report generating.

References

Arlene Casey, Emma Davidson, Michael Poon, Hang Dong, Daniel Duma, Andreas Grivas, Claire Grover, Víctor Suárez-Paniagua, Richard Tobin, William Whiteley, Honghan Wu, and Beatrice Alex. A systematic review of natural language processing applied to radiology reports. *BMC Medical Informatics and Decision Making*, 21(1):179, 2021. ISSN 1472-6947. doi:10.1186/s12911-021-01533-7. URL <https://doi.org/10.1186/s12911-021-01533-7>.

Guanxiong Liu, Tzu-Ming Harry Hsu, Matthew McDermott, Willie Boag, Wei-Hung Weng, Peter Szolovits, and Marzyeh Ghassemi. Clinically accurate chest x-ray report generation, 2019. URL <https://arxiv.org/abs/1904.02633>.

Tim Tanida, Philip Müller, Georgios Kaassis, and Daniel Rueckert. Interactive and explainable region-guided radiology report generation. In *Proceedings of the IEEE/CVF Conference on Computer Vision and Pattern Recognition (CVPR)*, pages 7433–7442, June 2023.

Shuxin Yang, Xian Wu, Shen Ge, Zhuozhao Zheng, S. Kevin Zhou, and Li Xiao. Radiology report generation with a learned knowledge base and multi-modal alignment. *Medical Image Analysis*, 86:102798, 2023. ISSN 1361-8415. doi:<https://doi.org/10.1016/j.media.2023.102798>. URL <https://www.sciencedirect.com/science/article/pii/S1361841523000592>.

Alexandros Karargyris, Satyananda Kashyap, Ismini Lourentzou, Joy T. Wu, Arjun Sharma, Matthew Tong, Shafiq Abedin, David Beymer, Vandana Mukherjee, Elizabeth A. Krupinski, and Mehdi Moradi. Creation and validation of a chest x-ray dataset with eye-tracking and report dictation for ai development. *Scientific Data*, 8(1):92, 2021. ISSN 2052-4463. doi:10.1038/s41597-021-00863-5. URL <https://doi.org/10.1038/s41597-021-00863-5>.

Ricardo Bigolin Lanfredi, Mingyuan Zhang, William F. Auffermann, Jessica Chan, Phuong-Anh T. Duong, Vivek Srikumar, Trafton Drew, Joyce D. Schroeder, and Tolga Tasdizen. REFLACX, a dataset of reports and eye-tracking data for localization of abnormalities in chest x-rays. *Scientific Data*, 9(1):350, 2022. ISSN 2052-4463. doi:10.1038/s41597-022-01441-z. URL <https://doi.org/10.1038/s41597-022-01441-z>.

Chong Ma, Hanqi Jiang, Wenting Chen, Yiwei Li, Zihao Wu, Xiaowei Yu, Zhengliang Liu, Lei Guo, Dajiang Zhu, Tuo Zhang, Dinggang Shen, Tianming Liu, and Xiang Li. Eye-gaze guided multi-modal alignment for medical representation learning. In A. Globerson, L. Mackey, D. Belgrave, A. Fan, U. Paquet, J. Tomczak, and C. Zhang, editors, *Advances in Neural Information Processing Systems*, volume 37, pages 6126–6153. Curran Associates, Inc., 2024. URL https://proceedings.neurips.cc/paper_files/paper/2024/file/0b9536e186a77feff516893a5f393f7a-Paper-Conference.pdf.

Yinbin Lu and Alan Wang. Integrating language into medical visual recognition and reasoning: A survey. *Medical Image Analysis*, 102:103514, 2025. ISSN 1361-8415. doi:<https://doi.org/10.1016/j.media.2025.103514>. URL <https://www.sciencedirect.com/science/article/pii/S1361841525000623>.

Kihyun You, Jawook Gu, Jiyeon Ham, Beomhee Park, Jiho Kim, Eun K. Hong, Woonhyuk Baek, and Byungseok Roh. Cxr-clip: Toward large scale chest x-ray language-image pre-training. In Hayit Greenspan, Anant Madabhushi, Parvin Mousavi, Septimiu Salcudean, James Duncan, Tanveer Syeda-Mahmood, and Russell Taylor, editors, *Medical Image Computing and Computer Assisted Intervention – MICCAI 2023*, pages 101–111, Cham, 2023. Springer Nature Switzerland. ISBN 978-3-031-43895-0. doi:10.1007/978-3-031-43895-0_10. URL <https://github.com/kakaobrain/cxr-clip>.

Zifeng Wang, Zhenbang Wu, Dinesh Agarwal, and Jimeng Sun. Medclip: Contrastive learning from unpaired medical images and text. In *Proceedings of the Conference on Empirical Methods in Natural Language Processing (EMNLP)*, pages 3876–3887. Association for Computational Linguistics, 2022. doi:10.18653/v1/2022.emnlp-main.256. URL <https://aclanthology.org/2022.emnlp-main.256>.

Shruthi Bannur, Stephanie Hyland, Qianchu Liu, Fernando Pérez-García, Maximilian Ilse, Daniel C. Castro, Benedikt Boecking, Harshita Sharma, Kenza Bouzid, Anja Thieme, Anton Schwaighofer, Maria Wetscherek, Matthew P. Lungren, Aditya Nori, Javier Alvarez-Valle, and Ozan Oktay. Learning to exploit temporal structure for biomedical vision-language processing. In *Proceedings of the IEEE/CVF Conference on Computer Vision and Pattern Recognition (CVPR)*, pages 15016–15027, June 2023.

Xiaoman Zhang, Chaoyi Wu, Ya Zhang, Weidi Xie, and Yanfeng Wang. Knowledge-enhanced visual-language pre-training on chest radiology images. *Nature Communications*, 14(1):4542, 2023. ISSN 2041-1723. doi:10.1038/s41467-023-40260-7. URL <https://doi.org/10.1038/s41467-023-40260-7>.

Mingjian Li, Mingyuan Meng, Michael Fulham, David Dagan Feng, Lei Bi, and Jinman Kim. Enhancing medical vision-language contrastive learning via inter-matching relation modeling. *IEEE Transactions on Medical Imaging*, 44(6):2463–2476, 2025. doi:10.1109/TMI.2025.3534436.

Bin Wang, Hongyi Pan, Armstrong Aboah, Zheyuan Zhang, Elif Keles, Drew Torigian, Baris Turkbey, Elizabeth Krupinski, Jayaram Udupa, and Ulas Bagci. Gazegnn: A gaze-guided graph neural network for chest x-ray classification. In *Proceedings of the IEEE/CVF Winter Conference on Applications of Computer Vision (WACV)*, pages 2194–2203, January 2024.

Qi Chen, Yutong Xie, Biao Wu, Xiaomin Chen, James Ang, Minh-Son To, Xiaojun Chang, and Qi Wu. Act like a radiologist: Radiology report generation across anatomical regions. In *Proceedings of the Asian Conference on Computer Vision (ACCV)*, pages 1–17, December 2024.

Yunsoo Kim, Jinge Wu, Su Hwan Kim, Pardeep Vasudev, Jiashu Shen, and Honghan Wu. Look & mark: Leveraging radiologist eye fixations and bounding boxes in multimodal large language models for chest X-ray report generation. In Wanxiang Che, Joyce Nabende, Ekaterina Shutova, and Mohammad Taher Pilehvar, editors, *Findings of the Association for Computational Linguistics: ACL 2025*, pages 17680–17694, Vienna, Austria, July 2025. Association for Computational Linguistics. ISBN 979-8-89176-256-5. URL <https://aclanthology.org/2025.findings-acl.909/>.

Benedikt Boecking, Naoto Usuyama, Sruthi Bannur, Daniel Coelho de Castro, Anton Schwaighofer, Stephanie Hyland, Himanshu Sharma, Moritz T. Wetscherek, Tristan Naumann, Aditya Nori, Javier Alvarez Valle, Hoifung Poon, and Ozan Oktay. Ms-cxr: Making the most of text semantics to improve biomedical vision-language processing. PhysioNet, 2024. URL <https://doi.org/10.13026/9g2z-jg61>. RRID:SCR_007345.

Yunze Liu, Qingnan Fan, Shanghang Zhang, Hao Dong, Thomas Funkhouser, and Li Yi. Contrastive multimodal fusion with tupleinfonce. In *Proceedings of the IEEE/CVF International Conference on Computer Vision (ICCV)*, pages 754–763, October 2021.

Nasir Hayat, Krzysztof J. Geras, and Farah E. Shamout. Medfuse: Multi-modal fusion with clinical time-series data and chest x-ray images. In Zachary Lipton, Rajesh Ranganath, Mark Sendak, Michael Sjoding, and Serena Yeung, editors, *Proceedings of the 7th Machine Learning for Healthcare Conference*, volume 182 of *Proceedings of Machine Learning Research*, pages 479–503. PMLR, 05–06 Aug 2022. URL <https://proceedings.mlr.press/v182/hayat22a.html>.

Alexey Dosovitskiy, Lucas Beyer, Alexander Kolesnikov, Dirk Weissenborn, Xiaohua Zhai, Thomas Unterthiner, Mostafa Dehghani, Matthias Minderer, Georg Heigold, Sylvain Gelly, Jakob Uszkoreit, and Neil Houlsby. An image is worth 16x16 words: Transformers for image recognition at scale. *CoRR*, abs/2010.11929, 2020. URL <https://arxiv.org/abs/2010.11929>.

Jeremy Irvin, Pranav Rajpurkar, Michael Ko, Yifan Yu, Silviana Ciurea-IIcus, Chris Chute, Henrik Marklund, Behzad Haghgoo, Robyn Ball, Katie Shpanskaya, Jayne Seekins, David A. Mong, Safwan S. Halabi, Jesse K. Sandberg, Ricky Jones, David B. Larson, Curtis P. Langlotz, Bhavik N. Patel, Matthew P. Lungren, and Andrew Y. Ng. Chexpert: a large chest radiograph dataset with uncertainty labels and expert comparison. In *Proceedings of the Thirty-Third AAAI Conference on Artificial Intelligence and Thirty-First Innovative Applications of Artificial Intelligence Conference and Ninth AAAI Symposium on Educational Advances in Artificial Intelligence*, AAAI’19/IAAI’19/EAAI’19. AAAI Press, 2019. ISBN 978-1-57735-809-1. doi:10.1609/aaai.v33i01.3301590. URL <https://doi.org/10.1609/aaai.v33i01.3301590>.

Emily Alsentzer, John Murphy, William Boag, Wei-Hung Weng, Di Jindi, Tristan Naumann, and Matthew McDermott. Publicly available clinical BERT embeddings. In Anna Rumshisky, Kirk Roberts, Steven Bethard, and Tristan Naumann, editors, *Proceedings of the 2nd Clinical Natural Language Processing Workshop*, pages 72–78, Minneapolis, Minnesota, USA, June 2019. Association for Computational Linguistics. doi:10.18653/v1/W19-1909. URL <https://aclanthology.org/W19-1909/>.

Aaron van den Oord, Yazhe Li, and Oriol Vinyals. Representation learning with contrastive predictive coding, 2019. URL <https://arxiv.org/abs/1807.03748>.

Michael U. Gutmann and Aapo Hyvärinen. Noise-contrastive estimation of unnormalized statistical models, with applications to natural image statistics. *J. Mach. Learn. Res.*, 13(1):307–361, February 2012. ISSN 1532-4435.

Jacob Cohen. *Statistical Power Analysis for the Behavioral Sciences*. Routledge, 2nd edition, 1988.

Zoya Bylinskii, Tilke Judd, Aude Oliva, Antonio Torralba, and Frédo Durand. What do different evaluation metrics tell us about saliency models? *IEEE Transactions on Pattern Analysis and Machine Intelligence*, 41(3):740–757, 2019.

R.J. Peters and L. Itti. Components of bottom-up gaze allocation in natural images. In *IEEE CVPR*, pages 1–7, 2005.

Wei Zhang and et al. Evaluating human gaze and model attention on glaucoma oct interpretation. *Medical Image Analysis*, 2024. In Press.

Chihcheng Hsieh, Chun Ouyang, Jacinto C. Nascimento, Joao Pereira, Joaquim Jorge, and Catarina Moreira. MIMIC-Eye: Integrating MIMIC Datasets with REFLACX and Eye Gaze for Multimodal Deep Learning Applications. <https://doi.org/10.13026/pc72-as03>, 2023. PhysioNet. RRID:SCR_007345.

Nicolas Riche, Matei Mancas, Thierry Dutoit, and Bernard Gosselin. Saliency and human fixations: State-of-the-art and study of comparison metrics. In *IEEE ICCV Workshops*, pages 1153–1160, 2013.

Kishore Papineni, Salim Roukos, Todd Ward, and Wei-Jing Zhu. Bleu: a method for automatic evaluation of machine translation. In *Proceedings of the 40th Annual Meeting on Association for Computational Linguistics*, ACL ’02, page 311–318, USA, 2002. Association for Computational Linguistics. doi:10.3115/1073083.1073135. URL <https://doi.org/10.3115/1073083.1073135>.

Chin-Yew Lin. ROUGE: A package for automatic evaluation of summaries. In *Text Summarization Branches Out*, pages 74–81, Barcelona, Spain, July 2004. Association for Computational Linguistics. URL <https://aclanthology.org/W04-1013/>.

Satanjeev Banerjee and Alon Lavie. METEOR: An automatic metric for MT evaluation with improved correlation with human judgments. In Jade Goldstein, Alon Lavie, Chin-Yew Lin, and Clare Voss, editors, *Proceedings of the ACL Workshop on Intrinsic and Extrinsic Evaluation Measures for Machine Translation and/or Summarization*, pages 65–72, Ann Arbor, Michigan, June 2005. Association for Computational Linguistics. URL <https://aclanthology.org/W05-0909/>.

Tianyi Zhang*, Varsha Kishore*, Felix Wu*, Kilian Q. Weinberger, and Yoav Artzi. Bertscore: Evaluating text generation with bert. In *International Conference on Learning Representations*, 2020. URL <https://openreview.net/forum?id=SkeHuCVFDr>.

Daniel Deutsch, George Foster, and Markus Freitag. Ties matter: Meta-evaluating modern metrics with pairwise accuracy and tie calibration. In Houda Bouamor, Juan Pino, and Kalika Bali, editors, *Proceedings of the 2023 Conference on Empirical Methods in Natural Language Processing*, pages 12914–12929, Singapore, December 2023. Association for Computational Linguistics. doi:10.18653/v1/2023.emnlp-main.798. URL <https://aclanthology.org/2023.emnlp-main.798>.

Saahil Jain, Ashwin Agrawal, Adriel Saporta, Steven QH Truong, Du Nguyen Duong, Tan Bui, Pierre Chambon, Yuhao Zhang, Matthew P. Lungren, Andrew Y. Ng, Curtis P. Langlotz, and Pranav Rajpurkar. Radgraph: Extracting clinical entities and relations from radiology reports, 2021. URL <https://arxiv.org/abs/2106.14463>.

Junting Pan, Kevin McGuinness, Elisa Sayrol, Noel E. O’Connor, and Xavier Giró-i-Nieto. Shallow and deep convolutional networks for saliency prediction. *CoRR*, abs/1603.00845, 2016. URL <http://arxiv.org/abs/1603.00845>.

R. A. Fisher. *Statistical Methods for Research Workers*, pages 66–70. Springer New York, New York, NY, 1992. ISBN 978-1-4612-4380-9. doi:10.1007/978-1-4612-4380-9_6. URL https://doi.org/10.1007/978-1-4612-4380-9_6.

M.L. Menéndez, J.A. Pardo, L. Pardo, and M.C. Pardo. The jensen-shannon divergence. *Journal of the Franklin Institute*, 334(2):307–318, 1997. ISSN 0016-0032. doi:[https://doi.org/10.1016/S0016-0032\(96\)00063-4](https://doi.org/10.1016/S0016-0032(96)00063-4). URL <https://www.sciencedirect.com/science/article/pii/S0016003296000634>.

Olivier Le Meur and Thierry Baccino. Methods for comparing scanpaths and saliency maps: strengths and weaknesses. *Behavior Research Methods*, 45(1):251–266, 2013. ISSN 1554-3528. doi:10.3758/s13428-012-0226-9. URL <https://doi.org/10.3758/s13428-012-0226-9>.

Appendix A.1 MIMIC-Eye Dataset Specifications and Processing Details

A.1.1 Dataset Composition

Metric	Count	Description
Total Patients	3,192	Unique individuals in the dataset
REFLACX Records	2,617	Records annotated with REFLACX labels
Eye Gaze Records	1,100	Records with gaze-tracking information
Full Multimodal Records	63	Records containing image, REFLACX & gaze data

Table 4: Core dataset metrics.

File Type	Count	Description
JPG Images	6,292	Chest X-ray images in JPEG
CSV Files	113,043	Eye gaze and associated metadata
JSON Files	4,112	Structured reports and annotations

Table 5: File distribution across modalities.

A.1.2 Detailed Modality Analysis

Modality Combination	Count	% of Records
Image + REFLACX	2,653	69.9%
Image + Eye Gaze	1,037	28.4%
Full Multimodal (Image + REFLACX + Gaze)	63	1.7%
Image Only	0	0%

Table 6: Distribution of modality combinations.

REFLACX Annotations.

- Total REFLACX Records: 2,617
- Unique REFLACX Patients: 2,199
- REFLACX Records with Eye Gaze: 63 (2.4%)
- Dataset Coverage: 71.6% of total records

Eye-Gaze Tracking.

- Total Eye-Gaze Records: 1,100
- Unique Eye-Gaze Patients: 1,038
- Eye-Gaze Records with REFLACX: 63 (5.7%)
- Dataset Coverage: 30.1% of total records

A.1.3 Condition Filtering Strategy

We retained eight primary conditions (top section of Table A.1.3) and excluded the six tail classes for three complementary reasons:

1. **Statistical Power and Model Stability** - Each retained condition exceeds 10% prevalence, delivering at least 250 training samples and adequate positive cases for validation/testing. Tail classes fall below 5%, inflating variance and hindering robust multi-label optimisation.
2. **Clinical Relevance and Non-Redundancy** - The eight selected phenotypes represent the most common findings on portable CXRs in critical-care settings and are routinely used for triage. Several discarded labels (e.g., Consolidation, Fracture) are radiographically subsumed by broader retained categories such as Lung Opacity or Pleural Effusion, introducing label redundancy without tangible clinical benefit.
3. **Balanced Multi-Modal Coverage** - Full-multimodal studies ($n = 63$) overwhelmingly feature the eight kept conditions ($\geq 90\%$ coverage), whereas the six tail labels occur in only four fully multimodal cases. Retaining them would preclude meaningful gaze-condition alignment experiments.

This pruning preserves $>86\%$ of the original label information while yielding a balanced, interpretable, and computationally tractable dataset.

Condition	Total	% of Dataset
No Finding	1,130	33.9%
Lung Opacity	831	24.9%
Pleural Effusion	750	22.5%
Support Devices	686	20.6%
Cardiomegaly	624	18.7%
Atelectasis	593	17.8%
Edema	445	13.4%
Pneumonia	370	11.1%
Consolidation (Removed)	149	4.5%
Pneumothorax (Removed)	124	3.7%
Lung Lesion (Removed)	95	2.9%
Enlarged Cardiomediastinum (Removed)	68	2.0%
Fracture (Removed)	46	1.3%
Pleural Other (Removed)	31	0.9%

Table 7: Condition distribution in the MIMIC-Eye dataset. Eight high-prevalence conditions were retained for analysis, while six tail classes with low frequency were removed to ensure statistical power, clinical relevance, and balanced multimodal coverage (see Section A.1.3).

A.1.4 Inter-condition Correlation Matrix

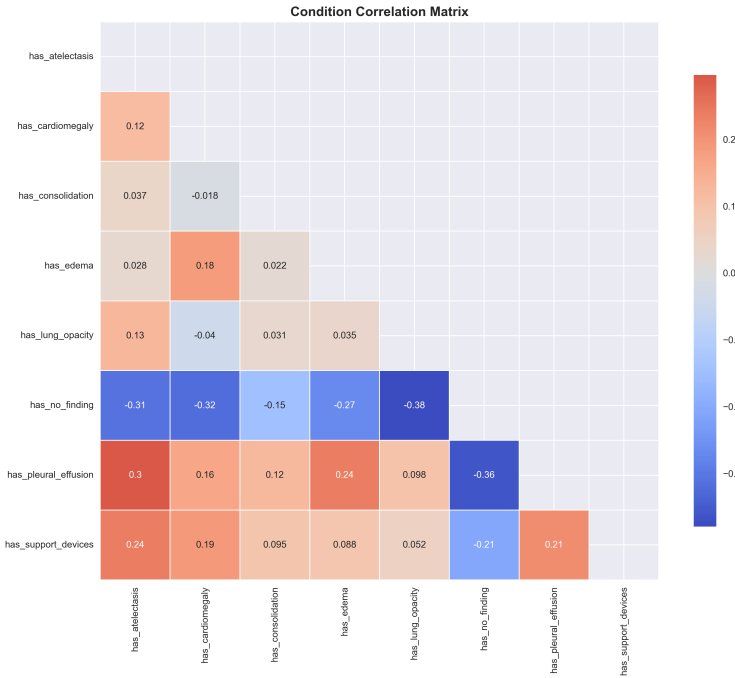


Figure 4: Pearson correlation coefficients between binary condition labels prior to pruning. Strong negative associations are observed between *No Finding* and all pathological classes (mean $\rho \approx -0.29$). Positive couplings are most pronounced for fluid-related findings such as Pleural Effusion -Edema ($\rho = 0.24$) and Atelectasis -Support Devices ($\rho = 0.24$).

A.1.5 Latent-space Structure via t-SNE

To visualise non-linear relationships in the CheXpert-initialised image feature space, we projected 3,654 study-level vectors into two dimensions using t-SNE (perplexity = 40, $\theta = 0.5$). The composite plot highlights global structure and class imbalance, while condition-specific overlays reveal pathology-dependent manifolds.

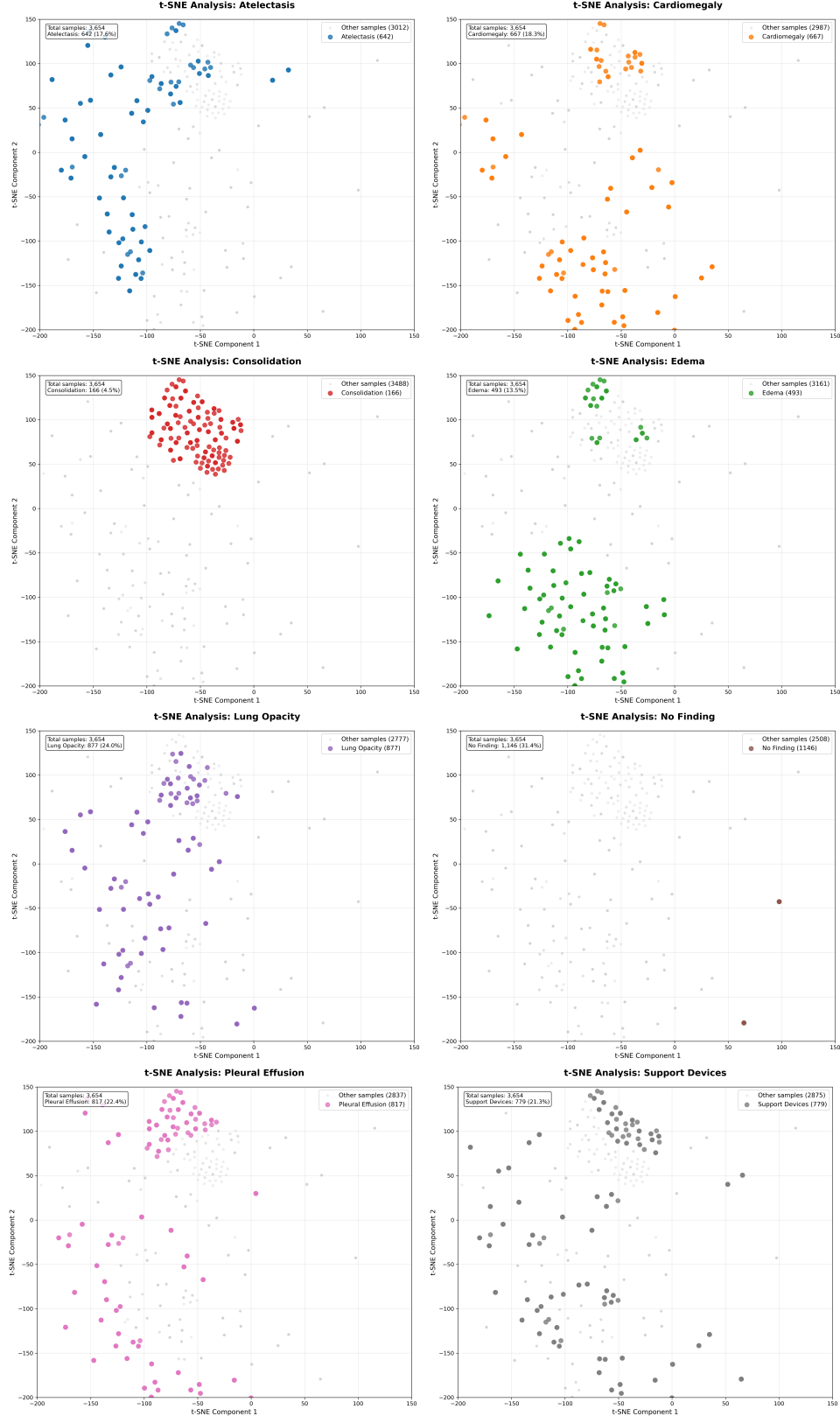


Figure 5: t-SNE class-specific overlays. Each subplot highlights the distribution of a given condition: (A.3) Atelectasis, (A.4) Cardiomegaly, (A.5) Consolidation, (A.6) Edema, (A.7) Lung Opacity, (A.8) No Finding, (A.9) Pleural Effusion, (A.10) Support Devices. Observed manifolds align with expected radiographic co-occurrences and variations.

A.1.6 Gaze Normalization Procedure

The REFLACX fixation dataset provides gaze coordinates in image pixel space ('x_position', 'y_position'), whereas the EyeGaze dataset records gaze as normalized screen coordinates ('FPOGX', 'FPOGY') in the range [0, 1]. To create a common dataset, we normalized REFLACX gaze values into the same [0, 1] coordinate system.

Step 1: Extract Image Bounds

REFLACX includes bounding boxes of the displayed image within the DICOM viewer:

- Image bounds: `xmin_shown_from_image`, `ymin_shown_from_image`, `xmax_shown_from_image`, `ymax_shown_from_image`.
- Screen bounds: `xmin_in_screen_coordinates`, `ymin_in_screen_coordinates`, `xmax_in_screen_coordinates`, `ymax_in_screen_coordinates`.

Step 2: Normalize REFLACX Gaze

We compute normalized gaze coordinates as:

$$x_{\text{norm}} = \frac{x_{\text{position}} - \text{xmin}_{\text{shown_from_image}}}{\text{xmax}_{\text{shown_from_image}} - \text{xmin}_{\text{shown_from_image}}}$$

$$y_{\text{norm}} = \frac{y_{\text{position}} - \text{ymin}_{\text{shown_from_image}}}{\text{ymax}_{\text{shown_from_image}} - \text{ymin}_{\text{shown_from_image}}}$$

Values outside [0, 1] due to calibration noise are clipped.

Step 3: Alignment with EyeGaze

EyeGaze coordinates ('FPOGX', 'FPOGY') are already normalized in screen space. After normalization, both datasets represent gaze positions in the same [0, 1] range, enabling direct comparison and fusion.

Step 4: Pupil Normalization

REFLACX provides a precomputed `pupil_area_normalized`. For EyeGaze, we estimate the pupil area from left and right pupil diameters:

$$A = \frac{\pi}{2} \left(\frac{LPD^2}{2} + \frac{RPD^2}{2} \right)$$

We then normalize pupil area relative to a baseline average computed over the first 1–2 seconds of valid gaze data.

Step 5: Fixation Duration

Fixation duration is derived as:

$$d = \text{timestamp}_{\text{end_fixation}} - \text{timestamp}_{\text{start_fixation}}$$

for REFLACX, and directly from FPOGD for EyeGaze.

Outcome

After these steps, both REFLACX and EyeGaze datasets share the following common fields:

- Normalized gaze position: $(x_{\text{norm}}, y_{\text{norm}})$
- Pupil area (normalized)
- Fixation duration
- Timestamp

This harmonization ensures comparability of gaze features across datasets.

A.2 Hyperparameter Settings

Enhanced gaze models. Learning rate 6×10^{-6} ; epochs 40; cosine scheduler with warmup; batch size 32 (or 8 on low-memory systems).

Model	Learning rate	Batch size	Epochs	Scheduler
Enhanced-gaze (ours)	6×10^{-6}	32	40	Cosine + warmup
MIMIC baseline	5×10^{-6}	32	35	Cosine
ViT-only	5×10^{-5}	128	20	Cosine

Table 8: Training schedules used across model variants.

Optimizer (AdamW)	Value	Notes
β_1	0.9	
β_2	0.98	
ϵ	1×10^{-8}	
Weight decay	<i>per-run arg</i>	As set in training arguments
Gradient clipping	0.4	<code>max_grad_norm = 0.4</code>

Table 9: Optimizer and regularization configuration.

Bounding Box Completion using YOLOv8n for REFLACX Data

We developed an enhanced bounding box completion framework that integrates radiologist-provided REFLACX annotations with predictions from **YOLOv8n** to achieve comprehensive spatial coverage in chest X-rays. The framework ensures both clinical fidelity and computational efficiency, while providing standardized representations suitable for multimodal medical AI models. A total of 17 anatomical regions were defined to consistently capture the thoracic cavity. This standardization addresses variability in annotation styles and facilitates uniform downstream processing. To preserve expert knowledge, REFLACX annotations are prioritized. YOLOv8n predictions are only used to fill missing or incomplete regions. This strategy ensures maximum coverage without overriding radiologist expertise. All completed bounding boxes are transformed into spatial attention masks. Gaussian smoothing is applied to generate soft anatomical boundaries, enabling more effective integration with multimodal models. A low confidence threshold of 0.05 was adopted to maximize medical sensitivity, while an IoU threshold of 0.5 was applied to manage overlapping regions. These thresholds were selected to balance recall of subtle findings with control over redundant detections. The framework employs memory-optimized inference for large-scale processing. Comprehensive quality control measures are implemented, including:

- **Spatial coverage metrics:** percentage of image area covered by annotations,
- **Anatomical completeness:** assessment of essential region coverage,
- **Confidence distribution analysis:** evaluation of detection reliability, and
- **Source attribution:** breakdown of contributions from REFLACX versus YOLOv8n.

This design provides richer and more standardized spatial context, enabling downstream multimodal models to benefit from improved spatial fidelity and clinical robustness.

A.3 Attention Metrics Thresholds and Report Generation Evaluation

Metric	Interpretation	Thresholds / Benchmarks
Pearson Correlation (r)	Measures linear alignment between human and AI attention maps.	$r \geq 0.30$ = moderate alignment (Cohen, 1988). $r \geq 0.50$ = strong alignment. Typical radiology gaze studies: 0.20 -0.40 acceptable (Cohen, 1988).
Mean Squared Error (MSE)	Pixel-wise distance between normalized human and AI attention maps.	No universal cutoff; lower is better. $MSE \leq 0.05$ generally indicates good alignment in saliency benchmarking (Pan et al., 2016).
P-value (statistical test)	Significance of AI -human correlation above chance.	$p < 0.05$ = statistically significant alignment. $p < 0.01$ = strong evidence against null hypothesis (Fisher, 1992).
Jensen -Shannon Divergence (JSD)	Distribution similarity of attention maps (bounded [0,1]).	$JSD < 0.20$ = strong similarity; 0.20 -0.40 = moderate similarity. Inter-radiologist $JSD \approx 0.45$ = human upper bound (MIMIC-Eye) (Menéndez et al., 1997).
Normalized Scanpath Saliency (NSS)	Measures how well model saliency coincides with fixation locations.	$NSS \geq 1.0$ = good human-level alignment (Le Meur and Bacchino, 2013). Values < 0.2 = weak, but still indicate non-random overlap.
Human Attention Entropy	Entropy of human fixation maps; reflects variability in gaze.	Typical radiology range: 9 -11 bits (clinical gaze studies). Values outside this may indicate atypical fixation patterns.
Model Attention Entropy	Entropy of AI saliency maps; reflects diversity of model focus.	Desirable range similar to human entropy (9 -11 bits). Large deviations suggest over- or under-concentration of attention.

Table 10: Interpretation and practical thresholds for attention alignment metrics. Thresholds are drawn from cognitive psychology, saliency benchmarking, and clinical gaze -AI alignment studies.

Metric	Purpose	Threshold Interpretation
BLEU-1 to BLEU-4	Measures n-gram precision; evaluates lexical overlap with reference reports	>0.20 indicates acceptable word-level match; >0.30 suggests good domain alignment
ROUGE-1 / ROUGE-2 / ROUGE-L	Recall-oriented metric capturing clinical phrase and sequence overlap	ROUGE-L F1 >0.25 considered reasonable for medical reports; higher recall (>0.35) desirable in impression section
Clinical Keyword Overlap	Alignment of disease-specific and anatomical terminology between generated and reference reports	Coverage $>70\%$ ensures core clinical terms preserved; lower overlap risks omission of key conditions
Sentence-BERT Similarity	Embedding-based contextual coherence across sections	Cosine similarity >0.80 indicates strong semantic alignment; 0.65–0.80 suggests partial but acceptable agreement

Table 11: Evaluation metrics and threshold interpretations for report generation

A.6 Clinical Knowledge Integration

A.6.1 Anatomical Region Mapping

To support anatomically grounded modeling, we defined **17 standardized chest X-ray regions** covering the cardiac, pulmonary, pleural, and mediastinal compartments. Each region is encoded with normalized bounding box coordinates and annotated with its

clinical significance. This design provides a consistent spatial reference system for integrating human knowledge with AI attention mechanisms.

Region	Definition	Clinical Significance
Cardiac silhouette	Heart border and mediastinal contour	Cardiomegaly, heart failure assessment
Left lung	Complete left pulmonary field	Primary site for pathology detection
Right lung	Complete right pulmonary field	Primary site for pathology detection
Left upper lung zone	Left lung above hilum level	Upper lobe pathology, TB predilection
Left mid lung zone	Left lung at hilum level	Middle lobe syndrome, lingular pathology
Left lower lung zone	Left lung below hilum level	Aspiration pneumonia, effusion
Right hilar structures	Right pulmonary vessels and bronchi	Lymphadenopathy, vascular congestion
Left hilar structures	Left pulmonary vessels and bronchi	Lymphadenopathy, vascular congestion
Right costophrenic angle	Right diaphragm -chest wall junction	Pleural effusion detection
Left costophrenic angle	Left diaphragm -chest wall junction	Pleural effusion detection
Upper mediastinum	Superior mediastinal compartment	Support devices, central lines
Trachea	Central airway structure	Endotracheal tube placement

Table 12: Standardized anatomical regions with definitions and clinical significance.

A.6.2 Condition-to-Region Clinical Knowledge Matrix

To integrate domain expertise, we constructed a **condition-to-region mapping matrix**. Each medical condition is linked to its *primary* and *secondary* anatomical regions, alongside an *attention weight* reflecting clinical importance. A textual rationale provides medical justification for the associations.

Condition	Primary Regions	Secondary Regions	Weight	Clinical Rationale
Atelectasis	Left lung, Right lung	Lower lung zones	0.8	Gravity-dependent collapse, post-operative complications
Cardiomegaly	Cardiac silhouette	Upper mediastinum	0.95	Heart size >50% thoracic width, CHF indicator
Edema	Left lung, Right lung	Hilar structures	0.7	Bilateral perihilar distribution, Kerley B lines
Lung opacity	Lung zones (upper/mid/lower)	Entire lungs	0.85	Consolidation, diffuse patterns
Pleural effusion	Costophrenic angles	Lower lung zones	0.9	Gravity-dependent fluid collection
Pneumonia	Upper and lower lung zones	Mid lung zones	0.8	Lobar or bronchopneumonia patterns
Support devices	Upper mediastinum, Cardiac silhouette, Trachea	Hilar structures	0.9	Central lines, ET tubes, pacemakers
No finding	Cardiac silhouette, Left lung, Right lung	Upper lung zones	0.6	Normal baseline anatomical assessment

Table 13: Clinical condition -to -region mapping with weights and rationale.

This structured mapping enables the multimodal model to align disease-specific reasoning with anatomically localized evidence, improving explainability and clinical coherence.

A.6.3 Report Template System and Model Outputs

This section documents the report generation framework, including the prompt template used for LLM-driven radiology reporting and representative outputs from different models for a given DICOM study.

A.6.3.1 Prompt Template

The following template was employed for all LLM-based report generation experiments. It integrates structured system instructions, clinical analysis data, and task-specific instructions to ensure consistent reporting style and lexical alignment with expert references.

```

# Medical Report Generation Prompt Template

## Overview

This document contains the complete prompt template used for generating medical
reports via Large Language Model (LLM) integration.

## Complete Prompt Structure

The prompt template consists of three main sections that are dynamically combined:

### 1. System Instruction

You are an expert radiologist with 20+ years of experience. Generate a concise,
accurate chest X-ray report based on AI predictions.

Your report uses AI model predictions to generate accurate radiological reports.
Use clear radiological terminology and anatomical specificity based on **model
predictions**.

### REPORTING GUIDELINES:

1. **AI PREDICTION ANALYSIS**
   - Use AI predictions as the primary source for findings
   - Correlate predictions with clinical knowledge
   - Prioritize high-confidence predictions in reporting

2. **CONFIDENCE-BASED REPORTING**
   - >70% = Report directly and confidently
   - 50-70% = Use appropriate clinical uncertainty
   - <50% = Do not report

3. **INCLUDE DEVICE FINDINGS**
   - Always describe any visible medical device (e.g. tubes, catheters, lines),
     even if incidental
   - Mention if the **tip** is not visible or fully imaged
   - Report device positioning and termination when visible

4. **USE PROVIDED TERMINOLOGY**
   - Prefer using **exact phrases** from 'CLINICAL KEYWORDS' to improve alignment
     with ground truth
   - When high-confidence keywords are provided, incorporate them verbatim when
     clinically appropriate

5. **AVOID OVER-HEDGING**
   - Do not say "subtle findings cannot be excluded" unless prediction confidence
     is mixed (50-70%)
   - If the study is normal and high confidence, use definitive phrases: "No
     focal consolidation, pleural effusion, or pneumothorax."
   - Be decisive when model confidence is high (>70%)

6. **STYLE & STRUCTURE**
   - Match expert radiologist tone
   - Avoid unnecessary hedging or speculation
   - Each section (FINDINGS, IMPRESSION) should be continuous text (no bullet
     points)
   - Include non-pathological findings such as tubes, lines, or structural
     anomalies

7. **ANATOMICAL SPECIFICITY**
   - Use precise anatomical terms when supported by high-confidence predictions
   - Reference specific lung zones, cardiac contours, and bony structures as
     appropriate
   - Always mention any visible medical device, line, or tube if present

```

```

REPORTING STYLE: {reporting_style}

### 2. Clinical Data Section

==== CLINICAL ANALYSIS DATA ===

    MODEL PREDICTIONS (Clinical Decision Basis):
    [Dynamic condition predictions with confidence scores]

    CLINICAL KEYWORDS (Condition-Based):
    [Dynamic keywords organized by condition and confidence level]

RELEVANT ANATOMICAL REGIONS (Condition-Based):

[Dynamic anatomical regions mapped to predicted conditions]

[Optional: Patient Information section if provided]
    PATIENT INFORMATION:
- [Dynamic patient data fields]

### 3. Task Instruction Section

==== REPORTING TASK ===
Generate a [TEMPLATE_STYLE] with sections: [SECTIONS]

    SPECIFIC INSTRUCTIONS FOR THIS CASE:
    [Dynamic case-specific instructions based on predictions]

### FORMATTING INSTRUCTIONS:
- Structure:

FINDINGS:
[continuous paragraph]

IMPRESSION:
[continuous paragraph]

### INPUT STRUCTURE:
- 'CLINICAL KEYWORDS': Use exact phrases when clinically appropriate to maximize alignment
- 'MODEL PREDICTIONS': Primary guide - use to focus attention and generate findings
- 'RELEVANT ANATOMICAL REGIONS': Reference these locations when describing findings

### OPTIMIZATION GOALS:
- **Maximize lexical similarity** to expert reference reports
- **Use provided terminology verbatim** when possible
- **Include device findings** (tubes, catheters, lines) even if incidental
- **Be anatomically specific** when high-confidence predictions support it

EXAMPLE REPORT FORMATS:

Example 1 (Device Present):
FINDINGS:
Feeding tube extends into the upper abdomen, the tip is not imaged. Lung volumes are normal. Mediastinal contours and heart size within normal limits. No consolidation or pleural effusion. No pneumothorax. No acute osseous abnormality.

IMPRESSION:
No acute cardiopulmonary process.

Example 2 (Multiple Findings):

```

FINDINGS:

PA and lateral views of the chest demonstrate well-expanded lungs. In comparison to the prior study, there is interval obscuration of the right heart border and the medial right hemidiaphragm. Correlation with the lateral view suggests that this is likely due to interval development of small bilateral pleural effusions. Underlying consolidation is not excluded. No pneumothorax. Cardiomedastinal silhouette is otherwise stable.

IMPRESSION:

Interval development of small bilateral pleural effusions. Underlying consolidation not excluded.

Example 3 (Normal Study):

FINDINGS:

The lungs are hyperinflated reflective of COPD. Apparent increased opacity projecting over the right lung apex correlates with posterior right fifth rib fracture with callus. Streaky bibasilar opacities likely reflect atelectasis. No focal consolidation to suggest pneumonia. No pleural effusion or pneumothorax. The heart is normal in size, and the mediastinal contours are normal.

IMPRESSION:

No acute cardiopulmonary process. Focal opacity in the retrocardiac region.

****REMEMBER**:** Do NOT mention attention maps, saliency, heatmaps, or explainability data. Use model predictions and provided keywords only.

GOAL:

Maximize lexical and semantic similarity to the expert reference report. Prioritize clinical specificity and exact terminology alignment.

CHEST X-RAY REPORT:

/no_think

Dynamic Components

Condition Predictions Format

Condition: [CONDITION_NAME]

- Confidence: [XX.X%]
- Clinical Significance: [HIGH/MODERATE/LOW]
- Keywords: [relevant medical terms]

Clinical Keywords Format

High Confidence (>80%):

- [keyword1], [keyword2], [keyword3]

Moderate Confidence (60-80%):

- [keyword4], [keyword5], [keyword6]

Lower Confidence (40-60%):

- [keyword7], [keyword8], [keyword9]

Anatomical Regions Format

Primary Focus Areas:

- [anatomical_region_1]: [associated_condition]
- [anatomical_region_2]: [associated_condition]

Secondary Areas:

- [anatomical_region_3]: [associated_condition]

Report Templates

```

### Standard Template
- **Style:** "professional chest X-ray report"
- **Sections:** ["FINDINGS", "IMPRESSION"]
- **Length:** Moderate (2-4 sentences per section)

### Detailed Template
- **Style:** "comprehensive radiological analysis"
- **Sections:** ["FINDINGS", "IMPRESSION", "RECOMMENDATIONS"]
- **Length:** Extensive (4-6 sentences per section)

### Concise Template
- **Style:** "brief clinical summary"
- **Sections:** ["FINDINGS", "IMPRESSION"]
- **Length:** Brief (1-2 sentences per section)

## Key Safety Features

### Attention Data Prohibition
- **CRITICAL:** No mention of attention maps, saliency, heatmaps, or AI explainability
- Only use model predictions and clinical keywords
- Ensure reports are clinically safe and interpretable

### Confidence-Based Reporting
- High confidence (>70%): Direct reporting
- Moderate confidence (50-70%): Appropriate uncertainty language
- Low confidence (<50%): Do not report finding

### Medical Device Detection
- Always report visible medical devices
- Describe positioning and termination when visible
- Note if device tips are not visible or fully imaged

## Implementation Notes

### Dynamic Variables
- '{reporting_style}': Determined by case complexity
- '{template_config}': Based on selected template
- '{condition_predictions}': Live model outputs
- '{prediction_keywords}': Extracted clinical keywords
- '{relevant_anatomical_regions}': Mapped anatomical areas

### LLM Integration
- Compatible with LM Studio API
- Uses '/no_think' directive for direct response - specifically for qwen3
- Optimized for medical report generation models
- Supports both text-only and vision-language models

```

A.6.3.2 Ground Truth Report (Reference)

For DICOM ID **6c2b39fa-2c251fcf-addd31da-83faee60-044fa8f9**, the expert-provided reference report is:

Given Report:

FINAL REPORT

INDICATION: ___F with cirrhosis, recent PNA and alc hep presenting with fever 101.1 1 week ago. // evidence of PNA?

TECHNIQUE: PA and lateral views the chest.

COMPARISON: ___.

FINDINGS:

Enteric tube passes below the inferior field of view. The lungs are clear without consolidation, effusion or edema. The cardiomedastinal silhouette is within normal limits. No acute osseous abnormalities.

IMPRESSION:

Enteric tube in place. No focal consolidation.

Cleaned Report:

Findings: Enteric tube passes below the inferior field of view. The lungs are clear without consolidation, effusion or edema. The cardiomedastinal silhouette is within normal limits. No acute osseous abnormalities.

Impression: Enteric tube in place. No focal consolidation.

A.6.3.3 Model-Generated Reports**Gemini 2.5 Pro**

Findings: A gastric tube is seen extending into the upper abdomen with its tip likely within the stomach. The lungs are well-aerated. There is no focal consolidation, pleural effusion, or pneumothorax. The cardiac silhouette and mediastinal contours are within normal limits. The visualized osseous structures are unremarkable.

Impression: No acute cardiopulmonary process. A gastric tube is in place.

Qwen3

Findings: The chest radiograph demonstrates aerated lung fields without evidence of focal consolidation or pleural effusion in any zone. The cardiac silhouette is within normal limits. A gastric tube is visualized extending into the upper abdomen; however, the tip is not fully imaged. An additional lead is noted in the upper mediastinum. No acute osseous abnormalities are identified.

Impression: No acute cardiopulmonary process. A gastric tube and an additional lead are visualized.

Llama 4

Findings: The cardiac silhouette appears normal in size. Lung fields are aerated without focal consolidation or pleural effusion. A gastric tube is visible, extending into the upper abdomen, but its tip is not imaged. No acute infiltrates or opacities are seen.

Impression: No acute cardiopulmonary process identified. Clinical correlation is recommended regarding support devices.

MedGemma

Findings: The lungs are well-expanded bilaterally. No evidence of focal consolidation, pleural effusion, or pneumothorax. The cardiac silhouette and mediastinal contours are within normal limits. A gastric tube is visualized extending into the upper abdomen; the tip is not fully imaged. A laparoscopic gastric band is also noted.

Impression: No acute cardiopulmonary process. Visible support devices include a gastric tube and a laparoscopic gastric band.

BioMistral

Findings: A gastric tube is present in the upper abdomen, with the tip not imaged. The lungs are well-expanded bilaterally with no pleural effusion. Cardiomegaly is present. An acute infiltrate is seen in the left upper lung zone and a chronic infiltrate in the right lower lung zone.

Impression: Gastric tube present. Cardiomegaly and pulmonary infiltrates. No pleural effusion or pneumothorax.

A.6.3.4 Comparative Summary

Table 5 summarizes the alignment of model outputs with the ground truth report.

Model	Tube Detection	Lung Findings	Cardiac Findings	Extra/Hallucinated
Ground Truth	Yes	Clear	Normal silhouette	None
Gemini 2.5 Pro	Yes	Clear	Normal	None
Qwen3	Yes	Clear	Normal	Lead (hallucinated)
Llama 4	Yes	Clear	Normal	Suggests correlation
MedGemma	Yes	Clear	Normal	Laparoscopic band
BioMistral	Yes	Infiltrates (false)	Cardiomegaly (false)	Multiple findings

Table 14: Comparison of model-generated reports against ground truth reference.